

34 **Abstract**

35 The SARS-CoV-2 non-structural protein 1 (Nsp1) contains an N-terminal domain and C-terminal
36 helices connected by a short linker region. The C-terminal helices of Nsp1 (Nsp1-C-ter) from
37 SARS-CoV-2 bind in the mRNA entry channel of the 40S ribosomal subunit and blocks mRNA
38 entry, thereby shutting down host protein synthesis. Nsp1 suppresses host immune function and is
39 vital for viral replication. Hence, Nsp1 appears to be an attractive target for therapeutics. In this
40 study, we have *in silico* screened Food and Drug Administration (FDA)-approved drugs against
41 Nsp1-C-ter. Among the top hits obtained, montelukast sodium hydrate binds to Nsp1 with a binding
42 affinity (K_D) of $10.8 \pm 0.2 \mu\text{M}$ *in vitro*. It forms a stable complex with Nsp1-C-ter in simulation runs
43 with -95.8 ± 13.3 kJ/mol binding energy. Montelukast sodium hydrate also rescues the inhibitory
44 effect of Nsp1 in host protein synthesis, as demonstrated by the expression of firefly luciferase
45 reporter gene in cells. Importantly, it shows antiviral activity against SARS-CoV-2 with reduced
46 viral replication in HEK cells expressing ACE2 and Vero-E6 cells. We, therefore, propose
47 montelukast sodium hydrate can be used as a lead molecule to design potent inhibitors to help
48 combat SARS-CoV-2 infection.

49

50

51 INTRODUCTION

52

53 SARS-CoV-2, the causative agent of severe coronavirus disease-19 (COVID-19) pandemic, is an
54 enveloped positive-strand RNA-containing virus and belongs to beta coronavirus family (V'Kovski
55 et al., 2021). The virus contains nearly 30kb RNA genome with 5'-cap and 3' poly-A tail (Finkel et
56 al., 2021; V'Kovski et al., 2021). The SARS-CoV-2 genome encodes for fourteen open reading
57 frames (ORFs). Upon entry into host cells, ORF1a and ORF1b encode for two polyproteins, which
58 are later auto-proteolytically cleaved into sixteen proteins, namely Nsp1-Nsp16. Among these
59 proteins, Nsp1 binds in the mRNA entry channel of the 40S ribosomal subunit and blocks the entry
60 of mRNAs, thereby shutting down host protein synthesis. Nsp1 also induces endonucleolytic
61 cleavage of host RNAs (Kamitani et al., 2009).

62

63 The cryo-electron microscopy (cryo-EM) structures of ribosomes from Nsp1-transfected human
64 HEK293T cells indicate the binding of Nsp1 with 40S and 80S ribosomal subunits (Schubert et al.,
65 2020; Thoms et al., 2020; Tidu et al., 2020; Vankadari et al., 2020) (Figure 1-figure supplement
66 1A). Nsp1 contains 180 amino acids with N-terminal (1-127 amino acids) and C-terminal (148-180
67 amino acids) structured regions connected by a loop region of about 20 amino acids (Schubert et al.,
68 2020; Thoms et al., 2020) (Figure 1-figure supplement 1B). This C-terminal region of Nsp1 (Nsp1-
69 C-ter) contains two helices that harbours a conserved positively charged motif (KH-X₅-R/Y/Q-X₄-
70 R). The deposition of positive charge towards one edge of these helices enhances their ability to
71 bind helix h18 of 18S rRNA. The other side of C-terminal helices interacts with ribosomal proteins
72 uS3 and uS5 in mRNA entry tunnel of the 40S (Schubert et al., 2020; Thoms et al., 2020) (Figure
73 1-figure supplement 1A, zoomed view). These interactions enable Nsp1-C-ter to bind deep into the
74 mRNA entry tunnel and prevent the binding of mRNAs, thereby inhibiting host protein synthesis
75 (Schubert et al., 2020; Thoms et al., 2020; Tidu et al., 2020). Thus, Nsp1 helps in hijacking the host
76 translational machinery (Yuan et al., 2020) and renders the cells incapable of mounting an innate
77 immune response to counter the viral infection (Narayanan et al., 2008). Mutating the positively
78 charged residues K164 and H165 in Nsp1-C-ter to alanines leads to a decrease in binding affinity of
79 Nsp1 with ribosome and fails to inhibit host protein synthesis (Schubert et al., 2020; Thoms et al.,
80 2020; Tidu et al., 2020).

81

82 Nsp1 is a highly conserved protein and less than 3% of SARS-CoV-2 genomic sequences analysed
83 showed mutation in Nsp1 (Min et al., 2020). Further, Nsp1-C-ter showed a much reduced frequency
84 of mutations (Min et al., 2020). The crucial role of Nsp1 in inhibiting host gene expression,
85 suppression of host immune response (Narayanan et al., 2008) and, notably, the reduced mutation

86 frequency in Nsp1-C-ter across global SARS-CoV-2 genomes (Min et al., 2020) advocate targeting
87 Nsp1 for therapeutics. In this study, we have employed computational, biophysical, *in vitro* and
88 mammalian cell line based studies to identify FDA-approved drugs targeting Nsp1-C-ter and check
89 for its antiviral activity.

90

91 **RESULTS**

92 Since repurposing a drug is a quicker way to identify an effective treatment, we screened FDA-
93 approved drugs against Nsp1-C-ter (148-180 amino acids) which binds in the mRNA channel
94 (Figure 1-figure supplement 1C). The drugs docked to a small region of Nsp1-C-ter consisting of
95 residues (P153, F157, N160, K164, H165, and R171) which coincides with its ribosome-binding
96 interface (Figure 1-figure supplement 1C). The residues in Nsp1-C-ter involved in binding drugs
97 show minimal mutations in worldwide deposited 4,440,705 sequences of SARS-CoV-2 genome in
98 GISAID database (Figure 1-figure supplement 1D). We identified top hits with at least three
99 hydrogen bonds ;(H-bonds) near the ribosome binding site of Nsp1-C-ter (Supplementary File 1).
100 Further, the clash that the drugs may have against ribosome in its bound form with Nsp1-C-ter was
101 also analyzed. Montelukast sodium hydrate (hereafter referred to as montelukast) and saquinavir
102 mesylate (hereafter referred to as saquinavir) showed high clash scores (Supplementary File 1).
103 Montelukast is regularly used to make breathing easier in asthma (Paggiaro and Bacci, 2011), while
104 saquinavir is an anti-retroviral drug used in the treatment of human immunodeficiency virus
105 (HIV)(Khan et al., 2021).

106

107 Next, all twelve drugs were tested *in vitro* for their ability to bind to Nsp1. The purified proteins,
108 *i.e.*, full-length Nsp1 and C-terminal helices truncated Nsp1 (Nsp1 Δ C) proteins, were loaded on the
109 Ni-NTA sensors in BLI, and the compounds were screened to determine its binding to these
110 proteins. We found that montelukast and saquinavir show binding to Nsp1 (Figure 1A) but not with
111 Nsp1 Δ C (Figure 1B). This indicates that montelukast and saquinavir bind to Nsp1-C-ter. The rest of
112 the compounds does not show binding with Nsp1 or with Nsp1 Δ C (Figure 1A and 1B). We next
113 determined binding affinities of montelukast and saquinavir against Nsp1. Montelukast shows a
114 binding affinity (K_d) of $10.8 \pm 0.2 \mu\text{M}$ (Figure 1C) while saquinavir shows a binding affinity of
115 $7.5 \pm 0.5 \mu\text{M}$ towards Nsp1-C-ter (Figure 1D).

116

117 To further validate the binding of ligands with Nsp1-C-ter, we performed NanoDSF experiments
118 where we observed the change in the melting temperature of Nsp1 in the presence of drugs. We
119 observed that only montelukast and saquinavir induce a change in the melting temperature of Nsp1
120 (Figure 1-figure supplement 1E). None of the ligands were able to change the melting temperature

121 of the Nsp1 Δ C protein (Figure 1-figure supplement 1F). Next, we performed NanoDSF experiments
122 with different concentrations of montelukast and saquinavir to determine the change in melting
123 temperature of Nsp1. We observed that montelukast shifts the ΔT_m by 4.3°C while the saquinavir
124 causes a ΔT_m shift by 6.5°C (Figure 1E and F). Overall, montelukast and saquinavir showed binding
125 to Nsp1-C-ter *in vitro*.

126
127 To gain insights into the binding mode of montelukast and saquinavir with Nsp1-C-ter, we analyzed
128 the docked drugs and performed molecular dynamic simulation runs. The molecular screening
129 experiment shows the binding of montelukast with Nsp1-C-ter with a 5.61 docking score
130 (Supplementary File 1 and Figure 1-figure supplement 2A). In the simulation runs the root mean
131 square deviation (RMSD) of C-terminal helices bound with montelukast shows less deviation from
132 the mean atomic positions (Figure 1G). The analysis of H-bonds and hydrophobic interactions
133 indicate strong binding of montelukast during the simulation run. At the end of the simulation run,
134 montelukast shows a stable complex by forming H-bonds with E148 and L149, while F157 and
135 L173 form base stacking interactions (Figure 1H). The root mean square fluctuation (RMSF) plot
136 shows the thermal stability of individual residues throughout the molecular dynamics run of the
137 molecule, and it appears to be stable (Figure 1-figure supplement 2B). Saquinavir shows binding
138 with Nsp1 with a docking score of 5.6 (Supplementary File 1 and Figure 1-figure supplement 2C).
139 The RMSD plot of saquinavir bound C-terminal helices shows reduced deviation of the protein
140 atoms during the simulation runs from the mean atomic position (Figure 1I). The residues T151,
141 M174 and R175 form H-bonds with saquinavir while R171 forms base stacking interaction at the
142 end of the run (Figure 1J). The RMSF plot show that the participating residues is also stabilised
143 upon the binding of saquinavir (Figure 1-figure supplement 2D). Overall, the residues involved in
144 binding montelukast and saquinavir show extremely low mutational frequency.

145
146 Furthermore, these drug-Nsp1 complexes were subjected to free binding energy calculations using
147 End state free binding energy for 500 ns in two replicas for each complex. Montelukast and
148 saquinavir bind with Nsp1 with binding energies of -95.8 ± 13.3 kJ/mol and -42.7 ± 5.2 kJ/mol,
149 respectively. The average H-bonds were analysed for the C-terminal region of Nsp1 alone and drug-
150 bound complexes. We observed that these drugs-bound complexes show higher average H-bonds
151 throughout different replica simulations (Figure 1-figure supplement 2E).

152
153 Since Nsp1 is known to inhibit host protein synthesis by blocking the mRNA entry tunnel on the
154 ribosome and co-transfection of Nsp1 with capped luciferase reporter mRNA causes reduction of
155 luciferase expression (Thoms et al., 2020). We hypothesized that binding of montelukast or

156 saquinavir to Nsp1-C-ter may prevent inhibition of host protein synthesis. To test this hypothesis,
157 we carried out the cell-based translational rescue of luciferase activity in the presence of
158 montelukast and saquinavir in HEK293 cells when co-transfected with Nsp1. Co-transfection of
159 Nsp1 decreased the luciferase activity by almost half, which is restored by the increasing amount of
160 montelukast (Figure 2A). However, we do not observe a similar rescue of luciferase activity in the
161 presence of saquinavir (Figure 2B). Further experiments are needed to figure out why saquinavir is
162 unable to rescue the Nsp1-mediated translation inhibition. There was no significant change in gene
163 expression of the firefly luciferase *FLuc* gene (Figures 2C and 2D).

164
165 To test antiviral effects of montelukast and saquinavir against SARS CoV-2, we first tested the
166 cytotoxicity of these drugs in HEK293T-ACE2 and Vero-E6 cells. Results showed minimal toxicity
167 up to 10 μ M montelukast and saquinavir in both cell lines. However, in Vero-E6 cells, the highest
168 concentration (20 μ M) of both drugs showed an almost 80% decrease in cell viability, compared to
169 untreated cell control (Figure 3-figure supplement 1). Based on this, a working concentration of 10
170 μ M or lower was used for both drugs. At a concentration of 10 μ M, montelukast showed significant
171 antiviral activity, as indicated by reduced expression of viral spike protein in HEK293T-ACE2 and
172 Vero-E6 cells (Figures 3A and 3D). The corresponding qRT-PCR data demonstrated up to 1-log
173 reduction in viral copy number in both HEK293T-ACE2 and Vero-E6 cells at this concentration
174 (Figures 3B and 3E), supported by a decrease in infectious virus titer measured by plaque assay
175 (Figures 3C and 3F). No significant antiviral effects were observed in the presence of 10 μ M
176 saquinavir (Figure 3-figure supplement 2).

177

178 **DISCUSSION**

179 Nsp1 is a major virulence factor in SARS-CoV2 which effectively blocks the synthesis of major
180 immune effectors (IFN-beta, IFN- λ , and interleukin-8, retinoic acid-inducible gene I), thereby
181 aiding in establishment of the viral infection (Thoms et al., 2020). It serves as a blockage to host
182 mRNA entry by interacting with rRNA helix 18 and ribosomal proteins-uS5 and uS3 near the
183 mRNA entry channel of the 40S ribosomal subunit via its C-terminal helices (Thoms et al., 2020).
184 Structural studies on 48S-like preinitiation complex on Cricket paralysis viral internal ribosomal
185 entry site in presence of Nsp1 revealed its ability to lock the head domain of 40S ribosome in a
186 closed conformation. In addition, it competes with eIF3j for uS3 and weakens the binding of the
187 eIF3 to the 40S subunit (Yuan et al., 2020). While the host translation is inhibited by the C-terminal
188 helices of Nsp1, its N-terminal domain enhances translation of viral mRNAs by binding to the 5'
189 UTR (Shi et al., 2020). Moreover, Nsp1 interacts with host mRNA export receptor NXF1-NXT1
190 heterodimer and aids in retention of cellular mRNAs in the nucleus (Zhang et al., 2021). Further,

191 Mou et al., 2021 deciphered the frequency of mutation accumulation in the N-terminal domain was
192 higher than that of the C-terminal domain. Therefore, we targeted the C-terminal helices of Nsp for
193 this study.

194
195 Since repurposing a drug is a quicker way to identify an effective treatment, we screened FDA-
196 approved drugs against Nsp1-C-ter and found montelukast as potential lead molecule against it.
197 Montelukast is a leukotriene receptor antagonist and repurposing montelukast for tackling cytokine
198 storms in COVID-19 patients has been suggested (Sanghai and Tranmer, 2020) and hospitalized
199 COVID-19 patients that were given montelukast had significantly fewer events of clinical
200 deterioration (Khan et al., 2021). Montelukast also appears as a hit against the SARS-CoV-2 main
201 protease, (M^{pro}) protease, in computational studies (Abu-Saleh et al., 2020; Sharma et al., 2021).
202 However, Ma and Wang demonstrated that montelukast gives false positive anti-protease activity as
203 it cannot bind the GST-tagged-M^{pro} in thermal shift assay and native mass spectrometry
204 experiments (Ma and Wang, 2021). Thus, montelukast may not be an inhibitor for M^{pro} protease.

205 Viruses employ different strategies to shutdown host translation machinery. In SARS-CoV-2, Nsp1
206 inhibits translation by binding to the mRNA channel. Here, we show that montelukast binds to
207 Nsp1, rescues the Nsp1-mediated translation inhibition and has antiviral activity against SARS-
208 CoV-2. The rescue of shutdown of host protein synthesis machinery by montelukast seems to
209 contribute towards the antiviral activity of the drug; however, further experiments would be
210 essential to figure out detailed mechanism of its antiviral activity. Overall, our study identifies C-
211 terminal region of Nsp1 as a druggable target and montelukast as a starting point for designing more
212 potent drug molecules against SARS-CoV-2.

213 **Materials and Methods**

214 **Receptor preparation for *in silico* studies and molecular screening of FDA-approved drugs**

215 The three-dimensional coordinates of C-terminal helices of Nsp1 (Nsp1-C-ter; residue numbers 148
216 to 180) were taken from the cryo-EM structure of Nsp1-bound 40S (PDB ID: 6Z0J). The close
217 contacts, side chains, and bumps were fixed in Chimera (Pettersen et al., 2004). The molecule was
218 minimized using 100 steepest descent steps and ten conjugate gradient steps using AMBERff14SB
219 force field (Maier et al., 2015). None of the atoms were fixed during minimization, and charges
220 were assigned using the AMBERff14SB force field on standard residues. The final structure was
221 optimized by Powell method implemented in biopolymer programme of SYBYL-X v2.1 (Tripos
222 International, St. Louis, Missouri, 63144, USA).

223 The FDA-approved drug library was used to screen the drugs towards Nsp1-C-ter. The drug library
224 containing 1645 compounds was subjected to *in silico* molecular screening. Three-dimensional

225 structure of (SDF format) compound library was optimized in SYBYL-ligand prep module at
226 default parameters. The single lowest strain energy tautomer for each compound was searched using
227 Surflex in ligand preparation module. Subsequently, the binding pocket for ligands on Nsp1-C-ter
228 was determined by Computed Atlas of Surface Topography of proteins (CASTp) online server (Tian
229 et al., 2018). The T151, P153, D156, F157, Q158, N160, K164, H165, S167, T170, R171, E172,
230 L173, R175 and L177 were found to form the binding pocket. Finally, the compound library was
231 screened against 18S rRNA interacting interface of Nsp1-C-ter using the Surflex-dock program,
232 which is available in SYBYL v2.1 (Jain, 2003). Twenty conformers were generated for each
233 molecule with 100 maximum rotatable bonds, and top potential molecules were selected based on
234 docking score, which was calculated based on scoring function (flex C-score).

235

236 **Nsp1 expression and purification**

237 The gene construct encoding Nsp1 from SARS-CoV-2 in pCDNA 5-3X-Flag-Nsp1 was amplified
238 and sub-cloned into pET28a with N-terminal His-tag (Schubert et al., 2020; Thoms et al., 2020)
239 using appropriate primers (Supplementary File 2). The sub-cloned construct was further used to
240 amplify and clone the C-terminal 28 amino acid deleted construct of Nsp1 (Nsp1 Δ C) using
241 appropriate primers (Supplementary File 2). Then constructs were transformed into *E. coli* BL-21
242 DE3 expression system. The secondary cultures were then inoculated with 1% of the primary
243 culture and incubated at 37°C at 180 rpm. At 0.6 O.D., the cultures were induced with 1mM IPTG
244 at 16°C and 120 rpm for 18 Hrs. Cells were harvested at 6000 rpm and resuspended in buffer A (50
245 mM HEPES-KOH pH 7.6, 500 mM KCl, 5 mM MgCl₂, 5% Glycerol). Lysis was done by
246 sonicating at 18% amplitude (10 sec on/off cycles for 10 min) and clarified by centrifugation at
247 12000 rpm for 30 minutes. The clear supernatant was then loaded on the Ni-NTA beads (Qiagen)
248 and incubated for 3 Hrs, and beads were washed using buffer A. The bound protein was eluted with
249 buffer A supplemented with 300 mM imidazole, and purity was analysed on SDS-PAGE. The
250 fractions containing corresponding protein were concentrated and subjected to size exclusion
251 chromatography on Superdex 200 increase 10/300 column in buffer B (50 mM HEPES-KOH pH
252 7.6, 150 mM KCl, 5 mM MgCl₂, 2% Glycerol and 2 mM DTT). The pure protein fractions were
253 pooled and concentrated between 2-8 mg/ml and stored in -80 °C for further use.

254

255 **Drug-binding assays:**

256 ***Bio-layer Interferometry (BLI)***

257 To identify the kinetic behaviour of the top selected compounds, we performed the label-free
258 binding kinetics of protein and ligands by using bio-layer interferometry. The Ni-NTA sensors were
259 activated by incubating in 10 mM phosphate buffer saline for 10 min. Thereafter, 2 μ M of each

260 protein was loaded on the Ni-NTA sensor and a binding response of around 1 nm was obtained. The
261 initial screening of compounds was performed at 20 μM for all *in silico* selected top hits. The drug
262 molecules that showed binding response of more than 0.2 nm were chosen for further kinetic
263 experiments. The binding kinetics were measured by incubating protein-bound sensors with the
264 increasing ligand concentration (0-25 μM). The data for control sensors (without protein) for each
265 ligand concentration were also collected and subtracted from the response of proteins-bound
266 sensors. The subtracted data was then analysed by fitting the 1:1 stoichiometric ratio for association
267 and dissociation by applying the global fitting. Three independent experiments were performed to
268 evaluate the steady-state kinetics and calculate K_D values.

269

270 ***Nanoscale Differential Scanning Fluorometry (NanoDSF)***

271 *In silico* identified potential hits were then subjected to evaluate the binding with His-Nsp1 and His-
272 Nsp1 ΔC of SARS-CoV-2 protein. 2 μM of each protein was subjected to determine the melting
273 temperature the in buffer B. The temperature scans ranged from 20-90°C with the 1°C/min ramp
274 size using Prometheus NT.48 NanoTemper. Next, the ΔT_m was determined in the presence of drug
275 molecules (10 μM) to figure out binding of drug molecules. The top hits were selected for further
276 evaluation in a change of the T_m by incubating with different concentrations of ligand (0-16 μM).
277 The data was analysed by using ThermControl software.

278

279 **Molecular dynamics simulation of C-terminal helices of Nsp1 and drugs-bound complexes**

280 The molecular dynamic simulations of FDA-approved drugs in complex with Nsp1-C-ter were
281 selected based on top binding score using BLI and NanoDSF. The final docked complexes were
282 then prepared for molecular dynamics simulation studies. The systems for molecular dynamics
283 studies were prepared for Nsp1-C-ter alone and their complex with top hits using the Desmond
284 v4.1 implemented in Schrodinger-Maestro v11, where steric clashes and side-chain bumps were
285 fixed. These prepared structures were then optimized by GROMOS96 54a7 force field (Schmid et
286 al., 2011) and simple point charge water model was used to add the solvent molecules in
287 dodecahedron box with a distance of 1Å from the surface of protein. Additionally, four sodium ions
288 were added to neutralize the system. The following energy minimization was performed for all the
289 systems with 5000 steps of steepest descent and conjugate gradient algorithms with threshold
290 energy of 100 Kcal/mol. The systems were then equilibrated in two phases, first is isothermal-
291 isochoric equilibration, where constant number, volume, and temperature (NVT) was equilibrated
292 for 100 picoseconds (ps), and the temperature of the system was monitored for all constants. In
293 second phase, isothermal-isobaric equilibration was performed where number of particles, pressure,
294 and temperature (NPT) was equilibrated for 100 ps. After successful equilibration of the system,

295 final molecular dynamic runs were performed for 500 nanoseconds (ns) in three replicas with 2
296 femtoseconds of time steps. The root mean square deviation (RMSD), root mean square fluctuation
297 (RMSF), and three-dimensional coordinates for all atoms of protein and ligands were extracted to
298 analyse the molecular dynamics runs.

299

300 **Binding energy calculation**

301 The binding energy for protein and ligands were calculated by applying the gmx_Molecular
302 Mechanic and Poisson-Boltzmann Surface Area (gmx-MMPBSA) (Valdes-Tresanco et al., 2021).
303 Two subsequent 500 ns runs from MD simulations were further subjected to perform the
304 gmx_MMPBSA by using AmberTools21. The binding energy was decomposed into free binding
305 energy for drug molecules for 5000 frames. This binding energy calculation quantitatively provides
306 *in silico* biomolecular interaction between selected ligands and target protein. This binding energy
307 mainly constitutes the polar solvation energy, non-polar solvation energy and potential energy. The
308 free binding energy ($\Delta G_{\text{binding}}$) of the ligand was calculated by the following equation:

$$309 \Delta G_{\text{binding}} = (G_{\text{complex}}) - (G_{\text{receptor}}) - (G_{\text{ligand}})$$

310 Where $\Delta G_{\text{complex}}$ describes the Gibbs free energy of the complex, G_{receptor} and G_{ligand} are total energy
311 of protein and ligand, respectively.

312

313 **Luciferase-based assay: Translation inhibition and rescue experiments**

314 The luciferase based reporter assay was used to evaluate the target-specific action of drug
315 molecules. HEK293 cells were transfected with 100 ng/well of pGL3-Fluc plasmid using
316 Lipofectamine 2000 (Thermo Fisher Scientific) according to the manufacturer's protocol at around
317 75-90% confluency in a 96 well plate. The plasmid expressing Nsp1 protein (pcDNA 3.1-Nsp1) was
318 co-transfected at 100 ng/well concentration. The transfection was performed in the presence of
319 drugs montelukast and saquinavir at different concentrations. The cells were lysed 24 Hrs post-
320 transfection, and luciferase activity was measured by using Luciferase Reporter assay system
321 (Promega Corporation) in the GLoMax Explorer system (Promega Corporation).

322 The expression level of *FLuc* was measured, keeping Glyceraldehyde 3-phosphate dehydrogenase
323 (GAPDH) as the control. Total RNA from all conditions was isolated using the TRIzol as per the
324 user manual protocol. 0.5 μg of total RNA was used as a template for cDNA synthesis (RevertAid
325 First Strand cDNA synthesis kit using manufacturer's protocol), which was further used as template
326 to quantitate FLuc and GAPDH expression in the presence of appropriate primers as mentioned in
327 Supplementary File 2. The relative Ct values were monitored in the three replicates and relative fold
328 change in expression was calculated. The significance of the data was monitored by applying the

329 unpaired t-test through assuming Gaussian distribution parametric test by defining the statistical
330 significance $P < 0.5$.

331 To evaluate the total viral copy number, RNA from SARS CoV-2 infected cells was isolated using
332 TRIzol as per manufacturer's instructions, and equal amount of RNA used to determine the viral
333 load using AgPath-ID™ One-Step RT-PCR kit (AM1005, Applied Biosystems). The primers and
334 probes against SARS CoV-2 N-1 gene used are mentioned in Supplementary File 1. A standard
335 curve was made using SARS CoV-2 genomic RNA standards, which was used to determine viral
336 copy number from Ct values.

337

338 **Cells and virus**

339 The following cell lines were used in this study, namely, HEK293 (ATCC), HEK293T-ACE2
340 (HEK293T cells stably expressing human angiotensin-converting enzyme 2) (BEI Resources NR-
341 52511, NIAID, NIH. RRID: CVCL_A7UK) and Vero-E6 cells (CRL-1586, ATCC, RRID:
342 CVCL_0574). The authenticity of HEK293T-ACE2 and Vero-E6 cell lines was confirmed by
343 Certificate of Analysis from their respective sources. HEK293T-ACE2 are human embryonic
344 kidney 293T cells that express the human ACE2 receptor, which is required for SARS-CoV-2 entry.
345 HEK293T-ACE2 and Vero E6 cells are of human and primate origin respectively, and express
346 ACE2 receptor. All cell lines tested negative for mycoplasma contamination. Cells were cultured in
347 complete media prepared using Dulbecco's modified Eagle medium (12100-038, Gibco)
348 supplemented with 10% HI-FBS (16140-071, Gibco), 100 U/mL Penicillin-Streptomycin
349 (15140122, Gibco) and GlutaMAX™ (35050-061, Gibco).

350 SARS-CoV2 (Isolate Hong Kong/VM20001061/2020, NR-52282, BEI Resources, NIAID, NIH)
351 was propagated and quantified by plaque assay in Vero-E6 cells as described before (Case et al.,
352 2020).

353

354 **Cytotoxicity assay**

355 HEK293T-ACE2 cells were seeded in 0.1 mg/mL poly-L-lysine (P9155-5MG, Sigma-Aldrich)
356 coated 96-well plate to reach 70-80% confluency after 24 Hrs. Vero-E6 cells were seeded in a
357 regular 96 well plate to reach similar confluency. Cells were treated with 5, 10 and 20 μ M
358 montelukast or saquinavir in triplicates and incubated at 37°C/5% CO₂. After 48 Hrs, cytotoxicity
359 was measured using AlamarBlue™ Cell Viability Reagent (DAL 1025, Thermo Fisher) as per
360 manufacturer's instructions.

361

362 **Western Blot**

363 Cells were washed gently with 1X warm PBS (162528, MP Biomedicals), lysed using 1X Laemmli
364 buffer (1610747, BIO-RAD), and heated at 95°C before loading on to a 10% SDS-PAGE gel.
365 Separated proteins were transferred onto a PVDF membrane (IPVH00010, Immobilon-P; Merck)
366 and incubated for 2hr with blocking buffer containing 5% Skimmed milk (70166, Sigma-Aldrich) in
367 PBST (1X PBS containing 0.05% Tween 20 (P1379, Sigma-Aldrich)) for 2 Hrs at RT (room
368 temperature). The blots were then probed with SARS-CoV-2 spike antibody (NR-52947, BEI
369 Resources, NIAID, NIH) in blocking buffer for 12 Hrs at 4°C, followed by secondary Goat Anti-
370 Rabbit IgG antibody (ab6721, Abcam, RRID:AB_955447) incubation for 2 Hrs. Proteins were
371 detected using Clarity Western ECL Substrate (1705061, BIO-RAD). Actin was labelled using
372 antibody against beta-actin [AC-15] (HRP) (ab49900, Abcam, RRID: AB_867494). Relative
373 intensity of bands was quantified using imagej/Fiji.

374

375 **Virus infection**

376 HEK293T-ACE2 cells were seeded in poly-L-lysine coated 24-well plate to reach 80% confluency
377 at the time of infection. Vero-E6 cells were seeded in a regular 24 well plate to reach similar
378 confluency. Cells, in quadruplicates, were first pre-treated with 5 and 10 µM concentrations of
379 montelukast sodium hydrate (PHR1603, Merck) or saquinavir mesylate (1609829, Merck) for 3 Hrs
380 in complete media, washed and infected with 0.1 MOI (HEK ACE2) or 0.001 MOI (Vero-E6 cells)
381 SARS CoV-2. After 48 Hrs, cell culture supernatants were collected for plaque assay, and cells
382 were harvested for western blot analysis or processed for total RNA extraction using TRIzol
383 (15596018, Thermo Fisher). The drugs were present in the media for the entire duration of the
384 experiment.

385

386 **Plaque Assay**

387 Infectious virus particles from cell culture supernatants were quantified by plaque assay. Briefly,
388 Vero-E6 cells were seeded in 12-well cell culture dishes, and once confluent, cells were washed
389 with warm PBS and incubated with dilutions of cell culture supernatants in 100 µL complete
390 DMEM for 1 Hrs at 37 °C / 5% CO₂. The virus inoculum was then removed, and cells overlaid
391 with 0.6% Avicel (RC-591, Dupont) in DMEM containing 2% HI-FBS. After 48 Hrs incubation,
392 cells were fixed with 4% paraformaldehyde, and crystal violet (C6158, Merck) staining was done to
393 visualize the plaques.

394

395 **Plasmids**

396 pLVX-EF1alpha-SARS-CoV-2-nsp1-2xStrep-IRES-Puro expressing SARS CoV-2 NSP1 was a
397 kind gift from Prof. Nevan Krogan (Gordon et al., 2020). Other plasmids used in this study include

398 Plasmids pRL-TK (mammalian vector for weak constitutive expression of wild-type Renilla
399 luciferase), pGL4 (mammalian vector expressing firefly luciferase), pIFN- β Luc (IFN beta
400 promoter-driven firefly luciferase reporter). The plasmid pMTB242 pcDNA5 FRT-TO-3xFLAG-
401 3C-Nsp1_SARS2 was a kind gift from Prof. Ronald Beckmann.

402

403 **Supporting Information**

404 Supporting information contains four figures and two supplementary files.

405

406 **Acknowledgements**

407 This work was supported by Intermediate Fellowship from DBT-Wellcome Trust India Alliance to
408 TH (IA/I/17/2/503313). TH also thanks SERB for funds released under IRPHA (COVID-19 Life
409 Sciences; File Number:IPA/2020/000094). ST acknowledges funding from DBT-BIRAC grant
410 (BT/CS0007/CS/02/20) and DBT-Wellcome Trust India Alliance Intermediate Fellowship
411 (IA/I/18/1/503613). We acknowledge Swarnajayanti Fellowship from DST to SME (SB/SJF/2020-
412 21/18). The authors also acknowledge DBT-IISc Partnership Program Phase-II (BT/PR27952-
413 INF/22/212/2018) for support.

414

415 **Notes**

416 The authors declare no conflict of interest.

417

418 **Figure Legends**

419 **Figure 1: Screening and binding kinetics and molecular simulation dynamics runs of drugs** 420 **against Nsp1-C-ter**

421 A & B) BLI analysis for the initial screening of binding of the drugs with the (A) Nsp1 and (B)
422 Nsp1 Δ C proteins.

423 C & D) The kinetic behaviors of (C) montelukast and (D) saquinavir monitored using BLI by
424 incubating increasing concentration of the drug molecule (0-25 μ M) on the protein-bound sensors.
425 Montelukast shows a binding constant (K_D) of 10.8 \pm 0.8 μ M, while saquinavir binds with Nsp1-C-ter
426 with a K_D value of 7.5 \pm 0.5 μ M. (Error bars represent standard deviation of three replicates in (C)
427 and (D).

428 E & F) NanoDSF experiments to evaluate the change in the melting temperature of the Nsp1 by
429 incubating increasing concentration of (E) montelukast and (F) saquinavir. (The experiments were
430 performed in three replicates)

431 G) Simulation runs with montelukast show stable RMSD values for all replica throughout all
432 molecular dynamic simulation trajectories for 500ns.

433 H) The analysis of binding mode of montelukast at the end of 500ns shows stable binding with C-
434 terminal helices. The residues E148 and L149 form H-bonds with montelukast, while F157 and
435 L173 forms base stacking interactions.

436 I) Simulation runs with saquinavir show stable pattern in RMSD values throughout in all molecular
437 dynamic simulation trajectories for 500ns.
438 J) The analysis of binding mode of saquinavir at the end of 500ns shows stable binding with the C-
439 terminal helices. The residues T151, M174 and R175 form H-bonds with saquinavir, while R171
440 forms base stacking interactions.
441

442 **Figure 2: Translational rescue experiments in the presence of montelukast and saquinavir**

443 A) Luciferase-based reporter assay shows translational rescue of luciferase in the presence of
444 montelukast.

445 B) Luciferase-based reporter assay shows that saquinavir could not rescue the luciferase expression.
446 Error bars represent standard deviation of three replicates in (A) and (B).

447 C & D) The real-time PCR to quantitate the fold change of *F Luc* gene in comparison to GAPDH in
448 the presence of different concentration of the drug molecules. A) montelukast B) saquinavir. The
449 panel below provides the details of experimental conditions.

450 Error bars represent standard deviation of three replicates in (A) and (B). The significance of the
451 data was monitored by applying the unpaired t-test through assuming Gaussian distribution
452 parametric test by defining the statistical significance. **P < 0.01; ***P < 0.001; ****P < 0.0001.
453 The error bars represent the standard deviation.
454

455 **Figure 3: Montelukast shows antiviral activity against SARS-CoV-2.**

456 A) HEK ACE2 cells were pre-treated with 5 or 10 μ M montelukast and infected with 0.1 MOI
457 SARS CoV-2 for 48hr. Virus spike protein expression by western blot analysis, with corresponding
458 relative density of bands are shown.

459 B) Viral RNA copy number from infected cells was quantified by qRT PCR and C) infectious virus
460 titer from cell culture supernatants by plaque assay, respectively. Vero E6 cells were pre-treated
461 with 5 or 10 μ M montelukast and infected with 0.001 MOI SARS CoV-2 for 48 hr.

462 D) Virus spike protein expression by western blot analysis, with corresponding relative density of
463 bands.

464 E) Viral RNA copy number from infected cells was quantified by qRT PCR and F) infectious virus
465 titer from cell culture supernatants by plaque assay.

466 *P<0.05; **P<0.01; ***P<0.001; ****P<0.0001; ns-not significant, using one-way ANOVA with
467 Dunnett's multiple comparison test. Error bars represent standard deviation.
468

469 **Supplementary Figure Legends**

470
471 **Figure 1 figure supplement 1:** Screening of FDA-approved drugs against Nsp1 from SARS-CoV-
472 2 and NanoDSF experiments to evaluate the binding of top hits with the Nsp1 and Nsp1 Δ C.

473 A) The cryo-EM structure of the Nsp1-bound 40S ribosome (PDB:6ZOJ) shows the bound C-
474 terminal helices of Nsp1 into the mRNA entry tunnel. The positively charged amino acids forms
475 extensive interaction with h18 of 18S rRNA and the other side of the C-terminal helices interacts
476 with uS3 and uS5.

477 B) The structure of Nsp1 shows the presence of N-terminal structured region (PDB ID:7K7P) and
478 C-terminal helices connected by a loop.

479 C) Molecular screening of FDA-approved compounds led to identification of top hits. The docking
480 mode of top hits (drugs) with Nsp1-C-ter is shown.

481 D) The residues in Nsp1-C-ter involved in binding of selected drugs shows reduced mutational
482 frequency. The analysis was performed on the worldwide deposited sequences of SARS-CoV-2
483 genome in GISAID database. The GISAID contains 4,440,705 genome sequences and we analyzed
484 single nucleotide variants (SNV) for residues involved in drug binding. This analysis is performed
485 with the help of GESS database (Fang et al., 2021) .

486 E and F) The change in the melting temperature of (E) Nsp1 and (F) Nsp1 Δ C protein was
487 monitored in the presence of the selected molecules. The melting curve for apo-proteins are shown
488 in black color . Montelukast and saquinavir induce change in the melting temperature of Nsp1 while
489 none of the molecules show any difference in the melting temperature of Nsp1 Δ C protein.

490

491 **Figure 1 figure supplement 2: Structural dynamics of drug-bound complexes of Nsp1-C-ter.**

492 A) Molecular docking conformation of montelukast with Nsp1-C-ter.

493 B) The RMSF plot of montelukast- bound residues of Nsp1-C-ter during the different replica runs.

494 C) Molecular docking conformation of saquinavir with Nsp1-C-ter.

495 D) The RMSF plot of saquinavir- bound residues of Nsp1-C-ter during the different replica runs.

496 E) Average hydrogen bonds throughout the different replica of the simulation runs of Nsp1 and
497 drugs-bound complexes.

498

499 **Figure 3 figure supplement 1: Cytotoxicity assay**

500 Cells were treated in triplicates with increasing concentrations of montelukast or saquinavir as
501 indicated, and cytotoxicity of the drugs was tested 48hr later by Alamar Blue assay. Data shows
502 percentage toxicity of drugs compared to cell control in (A) HEK293T-ACE2 and (B) Vero E6 cells.
503 **P < 0.01; ***P < 0.001; ****P < 0.0001; ns - not significant, using one-way ANOVA with
504 Dunnett's multiple comparison test. Error bars represent standard deviation.

505

506 **Figure 3 figure supplement 2. Saquinavir did not show significant antiviral activity against**
507 **SARS-CoV-2.**

508 A) HEK ACE2 cells were pre-treated with 5 or 10 μ M saquinavir and infected with 0.1 MOI SARS
509 CoV-2 for 48hr. Virus spike protein expression by western blot analysis, with corresponding
510 relative density of bands are shown in (A).

511 B and C) Viral RNA copy number from infected cells was quantified by qRT PCR, and infectious
512 virus titer from cell culture supernatants by plaque assay, shown in (B) and (C) respectively.

513 D) Vero E6 cells were pre-treated with 5 or 10 μ M saquinavir and infected with 0.001 MOI SARS
514 CoV-2 for 48hr. Virus spike protein expression by western blot analysis, with relative density of
515 bands.

516 E and F) Viral RNA copy number from infected cells was quantified by qRT PCR and infectious
517 virus titer from cell culture supernatants by plaque assay.

518 **P < 0.01; ***P < 0.001; ****P < 0.0001; ns - not significant, using one-way ANOVA with
519 Dunnett's multiple comparison test. Error bars represent standard deviation.

520

521 **Supplementary Files Legends**

522

523 **Supplementary File 1:** Top hits of FDA-approved drugs upon screening against Nsp1-C-ter

524

525 **Supplementary File 2:** Primers /oligos used in this study

526

527

528 **References**

529

530 Abu-Saleh, A.A.A., Awad, I.E., Yadav, A., and Poirier, R.A. (2020). **Discovery of potent inhibitors**
531 **for SARS-CoV-2's main protease by ligand-based/structure-based virtual screening, MD**
532 **simulations, and binding energy calculations.** Physical chemistry chemical physics : PCCP 22,
533 23099-23106. <http://www.ncbi.nlm.nih.gov/pubmed/33025993> PubMed Google Scholar

534

535 Case, J.B., Bailey, A.L., Kim, A.S., Chen, R.E., and Diamond, M.S. (2020). **Growth, detection,**
536 **quantification, and inactivation of SARS-CoV-2.** Virology 548, 39-48.
537 <http://www.ncbi.nlm.nih.gov/pubmed/32838945> PubMed Google Scholar

538

539 Fang, S., Li, K., Shen, J., Liu, S., Liu, J., Yang, L., Hu, C.D., and Wan, J. (2021). **GESS: a**
540 **database of global evaluation of SARS-CoV-2/hCoV-19 sequences.** Nucleic acids research 49,
541 D706-D714. <http://www.ncbi.nlm.nih.gov/pubmed/33045727> PubMed Google Scholar

542

543 Finkel, Y., Mizrahi, O., Nachshon, A., Weingarten-Gabbay, S., Morgenstern, D., Yahalom-Ronen,
544 Y., Tamir, H., Achdout, H., Stein, D., Israeli, O., Beth-Din, A., Melamed, S., Weiss, S., Israely, T.,
545 Paran, N., Schwartz, M., and Stern-Ginossar, N. (2021). **The coding capacity of SARS-CoV-2.**
546 Nature 589, 125-130. <http://www.ncbi.nlm.nih.gov/pubmed/32906143> PubMed Google Scholar

547

548 Gordon, D.E., Jang, G.M., Bouhaddou, M., Xu, J., Obernier, K., White, K.M., O'Meara, M.J.,
549 Rezelj, V.V., Guo, J.Z., Swaney, D.L., Tummino, T.A., Huttenhain, R., Kaake, R.M., Richards, A.L.,
550 Tutuncuoglu, B., Foussard, H., Batra, J., Haas, K., Modak, M., Kim, M., Haas, P., Polacco, B.J.,
551 Braberg, H., Fabius, J.M., Eckhardt, M., Soucheray, M., Bennett, M.J., Cakir, M., McGregor, M.J.,
552 Li, Q., Meyer, B., Roesch, F., Vallet, T., Mac Kain, A., Miorin, L., Moreno, E., Naing, Z.Z.C., Zhou,
553 Y., Peng, S., Shi, Y., Zhang, Z., Shen, W., Kirby, I.T., Melnyk, J.E., Chorba, J.S., Lou, K., Dai, S.A.,
554 Barrio-Hernandez, I., Memon, D., Hernandez-Armenta, C., Lyu, J., Mathy, C.J.P., Perica, T., Pilla,
555 K.B., Ganesan, S.J., Saltzberg, D.J., Rakesh, R., Liu, X., Rosenthal, S.B., Calviello, L.,
556 Venkataramanan, S., Liboy-Lugo, J., Lin, Y., Huang, X.P., Liu, Y., Wankowicz, S.A., Bohn, M.,
557 Safari, M., Ugur, F.S., Koh, C., Savar, N.S., Tran, Q.D., Shengjuler, D., Fletcher, S.J., O'Neal, M.C.,
558 Cai, Y., Chang, J.C.J., Broadhurst, D.J., Klippsten, S., Sharp, P.P., Wenzell, N.A., Kuzuoglu-Ozturk,
559 D., Wang, H.Y., Trenker, R., Young, J.M., Caverio, D.A., Hiatt, J., Roth, T.L., Rathore, U.,
560 Subramanian, A., Noack, J., Hubert, M., Stroud, R.M., Frankel, A.D., Rosenberg, O.S., Verba, K.A.,
561 Agard, D.A., Ott, M., Emerman, M., Jura, N., von Zastrow, M., Verdin, E., Ashworth, A., Schwartz,
562 O., d'Enfert, C., Mukherjee, S., Jacobson, M., Malik, H.S., Fujimori, D.G., Ideker, T., Craik, C.S.,
563 Floor, S.N., Fraser, J.S., Gross, J.D., Sali, A., Roth, B.L., Ruggero, D., Taunton, J., Kortemme, T.,
564 Beltrao, P., Vignuzzi, M., Garcia-Sastre, A., Shokat, K.M., Shoichet, B.K., and Krogan, N.J. (2020).
565 **A SARS-CoV-2 protein interaction map reveals targets for drug repurposing.** Nature 583, 459-
566 468. <http://www.ncbi.nlm.nih.gov/pubmed/32353859> PubMed Google Scholar

567

568 Jain, A.N. (2003). **Surflex: fully automatic flexible molecular docking using a molecular**
569 **similarity-based search engine**. *Journal of medicinal chemistry* 46, 499-511.
570 <http://www.ncbi.nlm.nih.gov/pubmed/12570372> PubMed Google Scholar
571

572 Khan, A.R., Misdary, C., Yegya-Raman, N., Kim, S., Narayanan, N., Siddiqui, S., Salgame, P.,
573 Radbel, J., Groote, F., Michel, C., Mehnert, J., Hernandez, C., Braciale, T., Malhotra, J., Gentile,
574 M.A., and Jabbour, S.K. (2021). **Montelukast in hospitalized patients diagnosed with COVID-**
575 **19**. *The Journal of asthma : official journal of the Association for the Care of Asthma*, 1-7.
576 <http://www.ncbi.nlm.nih.gov/pubmed/33577360> PubMed Google Scholar
577

578 Ma, C., and Wang, J. (2021). **Dipyridamole, chloroquine, montelukast sodium, candesartan,**
579 **oxytetracycline, and atazanavir are not SARS-CoV-2 main protease inhibitors**. *Proceedings of*
580 *the National Academy of Sciences of the United States of America* 118.
581 <http://www.ncbi.nlm.nih.gov/pubmed/33568498> PubMed Google Scholar
582

583 Maier, J.A., Martinez, C., Kasavajhala, K., Wickstrom, L., Hauser, K.E., and Simmerling, C.
584 (2015). **ff14SB: Improving the Accuracy of Protein Side Chain and Backbone Parameters**
585 **from ff99SB**. *Journal of chemical theory and computation* 11, 3696-3713.
586 <http://www.ncbi.nlm.nih.gov/pubmed/26574453> PubMed Google Scholar
587

588 Min, Y.Q., Mo, Q., Wang, J., Deng, F., Wang, H., and Ning, Y.J. (2020). **SARS-CoV-2 nsp1:**
589 **Bioinformatics, Potential Structural and Functional Features, and Implications for**
590 **Drug/Vaccine Designs**. *Frontiers in microbiology* 11, 587317.
591 <http://www.ncbi.nlm.nih.gov/pubmed/33133055> PubMed Google Scholar
592

593 Narayanan, K., Huang, C., Lokugamage, K., Kamitani, W., Ikegami, T., Tseng, C.T., and Makino, S.
594 (2008). **Severe acute respiratory syndrome coronavirus nsp1 suppresses host gene expression,**
595 **including that of type I interferon, in infected cells**. *Journal of virology* 82, 4471-4479.
596 <http://www.ncbi.nlm.nih.gov/pubmed/18305050> PubMed Google Scholar
597

598 Paggiaro, P., and Bacci, E. (2011). **Montelukast in asthma: a review of its efficacy and place in**
599 **therapy**. *Therapeutic advances in chronic disease* 2, 47-58.
600 <http://www.ncbi.nlm.nih.gov/pubmed/23251741> PubMed Google Scholar
601

602 Pettersen, E.F., Goddard, T.D., Huang, C.C., Couch, G.S., Greenblatt, D.M., Meng, E.C., and
603 Ferrin, T.E. (2004). **UCSF Chimera--a visualization system for exploratory research and**
604 **analysis**. *Journal of computational chemistry* 25, 1605-1612.
605 <http://www.ncbi.nlm.nih.gov/pubmed/15264254> PubMed Google Scholar
606

607 Sanghai, N., and Tranmer, G.K. (2020). **Taming the cytokine storm: repurposing montelukast**
608 **for the attenuation and prophylaxis of severe COVID-19 symptoms**. *Drug discovery today* 25,
609 2076-2079. <http://www.ncbi.nlm.nih.gov/pubmed/32949526> PubMed Google Scholar
610

611 Schmid, N., Eichenberger, A.P., Choutko, A., Riniker, S., Winger, M., Mark, A.E., and van
612 Gunsteren, W.F. (2011). **Definition and testing of the GROMOS force-field versions 54A7 and**
613 **54B7**. *European biophysics journal : EBJ* 40, 843-856.
614 <http://www.ncbi.nlm.nih.gov/pubmed/21533652> PubMed Google Scholar
615

616 Schubert, K., Karousis, E.D., Jomaa, A., Scaiola, A., Echeverria, B., Gurzeler, L.A., Leibundgut,
617 M., Thiel, V., Muhlemann, O., and Ban, N. (2020). **SARS-CoV-2 Nsp1 binds the ribosomal**
618 **mRNA channel to inhibit translation**. *Nature structural & molecular biology* 27, 959-966.
619 <http://www.ncbi.nlm.nih.gov/pubmed/32908316> PubMed Google Scholar

620

621 Sharma, T., Abohashrh, M., Baig, M.H., Dong, J.J., Alam, M.M., Ahmad, I., and Irfan, S. (2021).
622 **Screening of drug databank against WT and mutant main protease of SARS-CoV-2: Towards**
623 **finding potential compound for repurposing against COVID-19.** Saudi journal of biological
624 sciences 28, 3152-3159. <http://www.ncbi.nlm.nih.gov/pubmed/33649700> PubMed Google Scholar

625

626 Thoms, M., Buschauer, R., Ameismeier, M., Koepke, L., Denk, T., Hirschenberger, M., Kratzat, H.,
627 Hayn, M., Mackens-Kiani, T., Cheng, J., Straub, J.H., Sturzel, C.M., Frohlich, T., Berninghausen,
628 O., Becker, T., Kirchhoff, F., Sparrer, K.M.J., and Beckmann, R. (2020). **Structural basis for**
629 **translational shutdown and immune evasion by the Nsp1 protein of SARS-CoV-2.** Science 369,
630 1249-1255. <http://www.ncbi.nlm.nih.gov/pubmed/32680882> PubMed Google Scholar

631

632 Tian, W., Chen, C., Lei, X., Zhao, J., and Liang, J. (2018). **CASTp 3.0: computed atlas of surface**
633 **topography of proteins.** Nucleic acids research 46, W363-W367.
634 <http://www.ncbi.nlm.nih.gov/pubmed/29860391> PubMed Google Scholar

635

636 Tidu, A., Janvier, A., Schaeffer, L., Sosnowski, P., Kuhn, L., Hammann, P., Westhof, E., Eriani, G.,
637 and Martin, F. (2020). **The viral protein NSP1 acts as a ribosome gatekeeper for shutting down**
638 **host translation and fostering SARS-CoV-2 translation.** Rna.
639 <http://www.ncbi.nlm.nih.gov/pubmed/33268501> PubMed Google Scholar

640

641 V'Kovski, P., Kratzel, A., Steiner, S., Stalder, H., and Thiel, V. (2021). **Coronavirus biology and**
642 **replication: implications for SARS-CoV-2.** Nature reviews Microbiology 19, 155-170.
643 <http://www.ncbi.nlm.nih.gov/pubmed/33116300> PubMed Google Scholar

644

645 Valdes-Tresanco, M.S., Valdes-Tresanco, M.E., Valiente, P.A., and Moreno, E. (2021).
646 **gmx_MMPBSA: A New Tool to Perform End-State Free Energy Calculations with**
647 **GROMACS.** Journal of chemical theory and computation 17, 6281-6291.
648 <http://www.ncbi.nlm.nih.gov/pubmed/34586825> PubMed Google Scholar

649

650 Vankadari, N., Jeyasankar, N.N., and Lopes, W.J. (2020). **Structure of the SARS-CoV-2 Nsp1/5'-**
651 **Untranslated Region Complex and Implications for Potential Therapeutic Targets, a Vaccine,**
652 **and Virulence.** The journal of physical chemistry letters 11, 9659-9668.
653 <http://www.ncbi.nlm.nih.gov/pubmed/33135884> PubMed Google Scholar

654

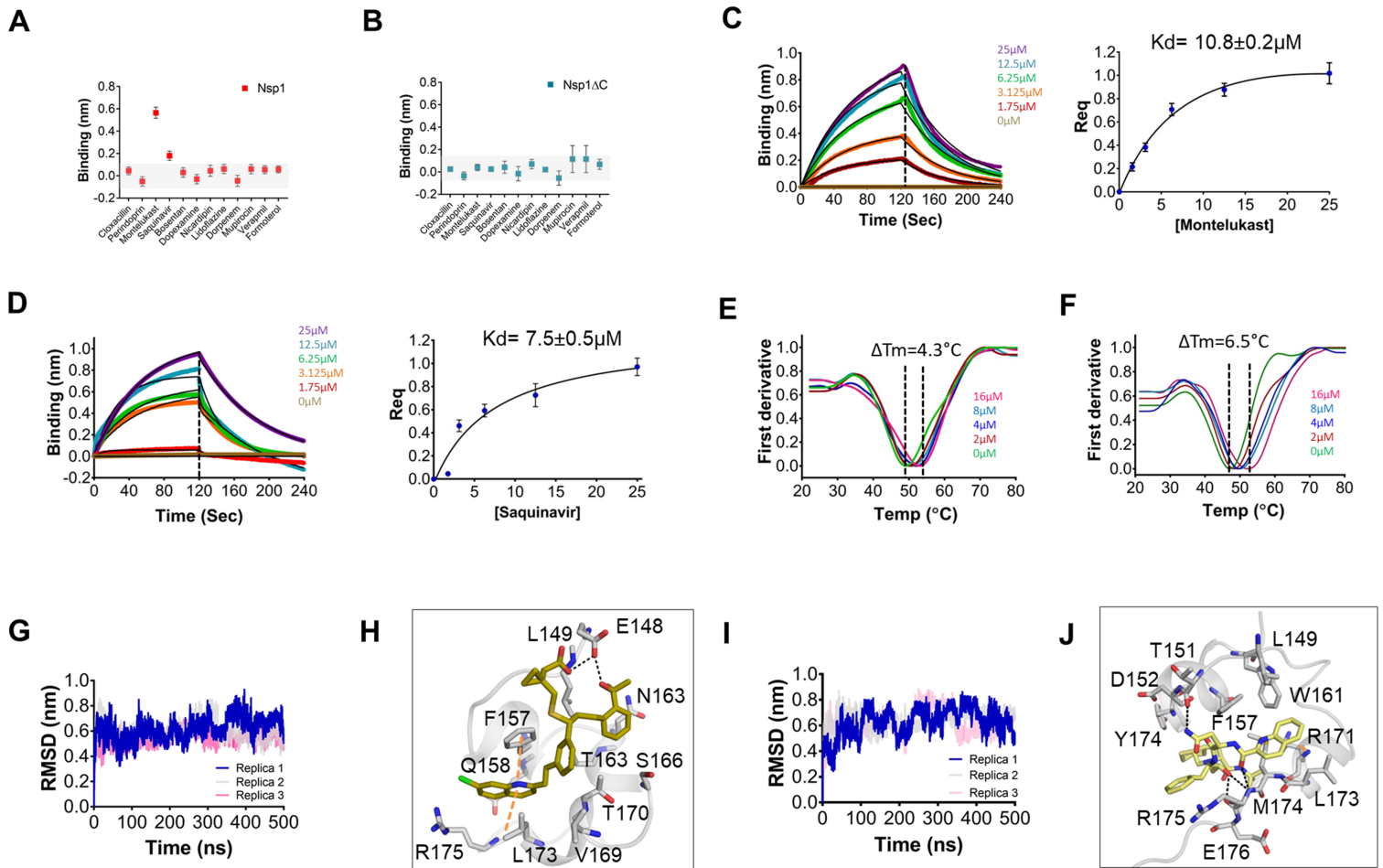
655 Yuan, S., Peng, L., Park, J.J., Hu, Y., Devarkar, S.C., Dong, M.B., Shen, Q., Wu, S., Chen, S.,
656 Lomakin, I.B., and Xiong, Y. (2020). **Nonstructural Protein 1 of SARS-CoV-2 Is a Potent**
657 **Pathogenicity Factor Redirecting Host Protein Synthesis Machinery toward Viral RNA.**
658 Molecular cell 80, 1055-1066 e1056. <http://www.ncbi.nlm.nih.gov/pubmed/33188728> PubMed
659 Google Scholar

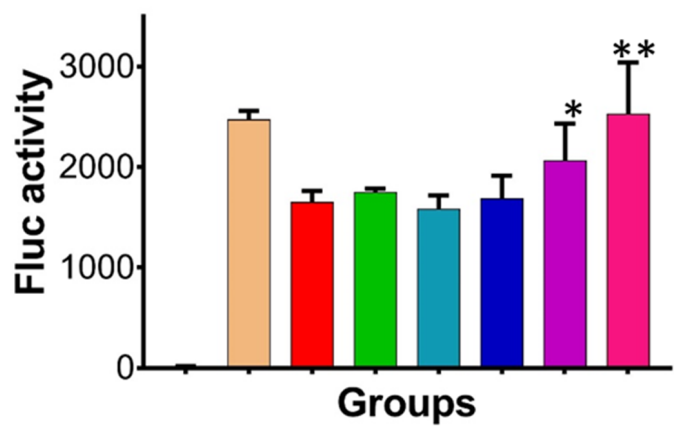
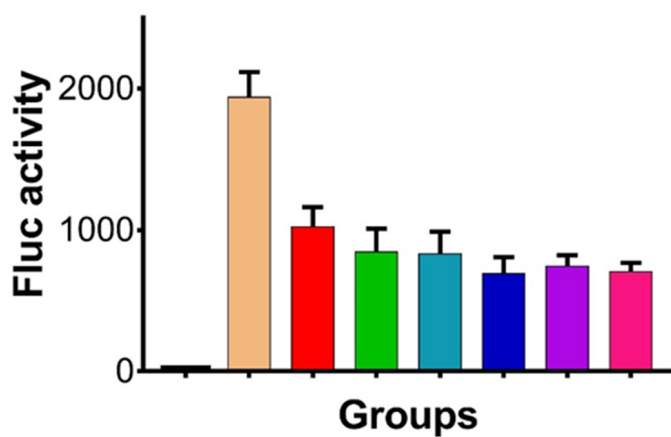
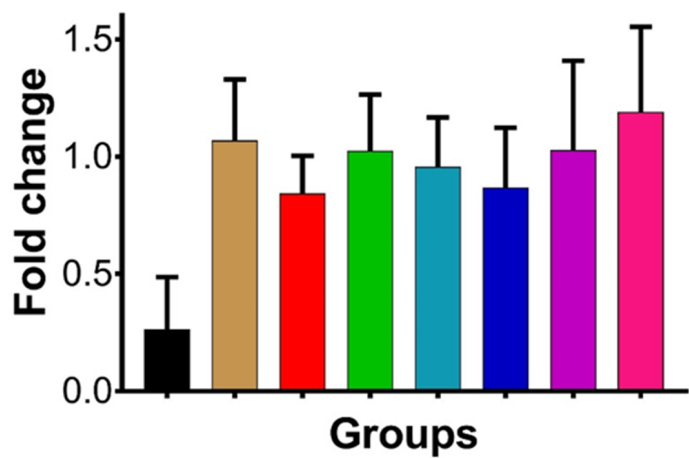
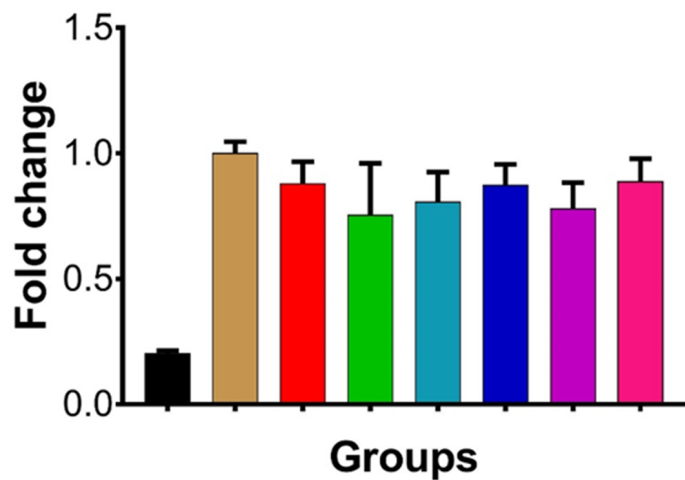
660

661 Zhang, K., Miorin, L., Makio, T., Dehghan, I., Gao, S., Xie, Y., Zhong, H., Esparza, M., Kehrer, T.,
662 Kumar, A., Hobman, T.C., Ptak, C., Gao, B., Minna, J.D., Chen, Z., Garcia-Sastre, A., Ren, Y.,
663 Wozniak, R.W., and Fontoura, B.M.A. (2021). **Nsp1 protein of SARS-CoV-2 disrupts the mRNA**
664 **export machinery to inhibit host gene expression.** Science advances 7.
665 <http://www.ncbi.nlm.nih.gov/pubmed/33547084> PubMed Google Scholar

666

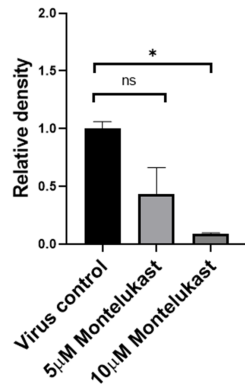
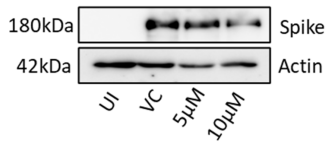
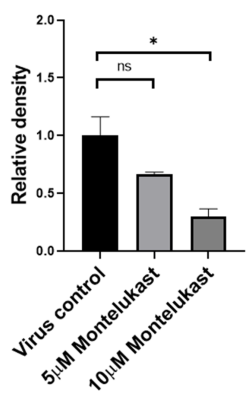
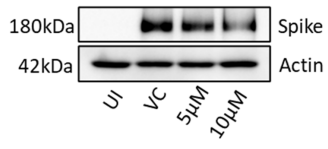
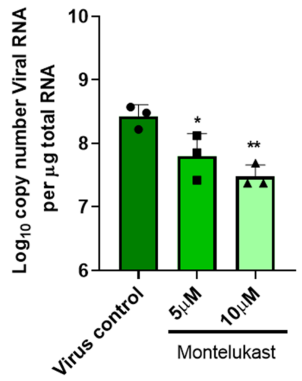
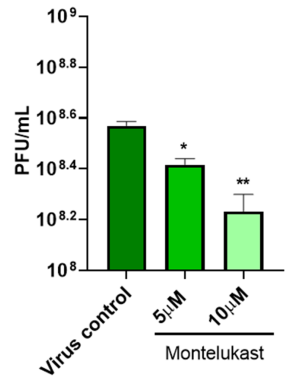
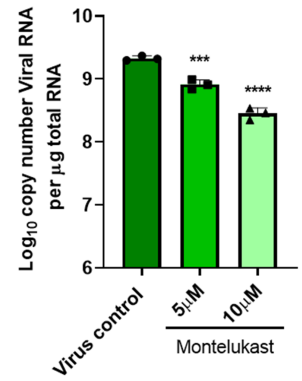
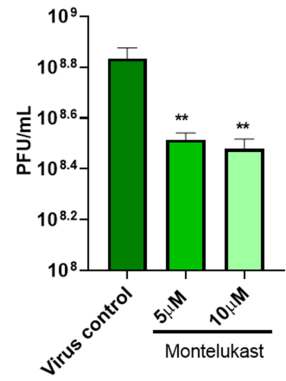
667

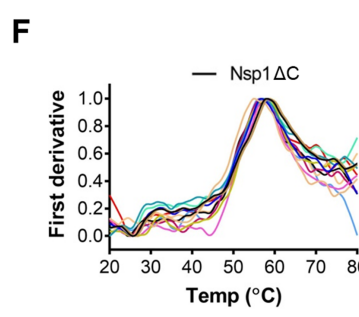
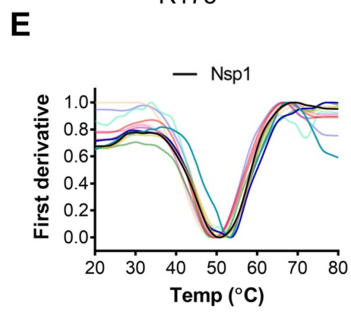
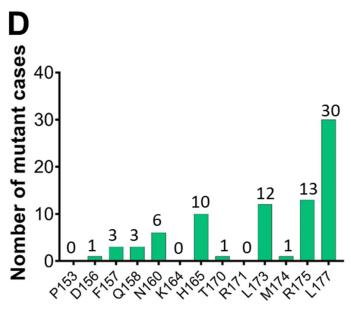
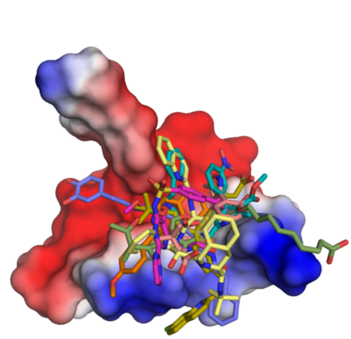
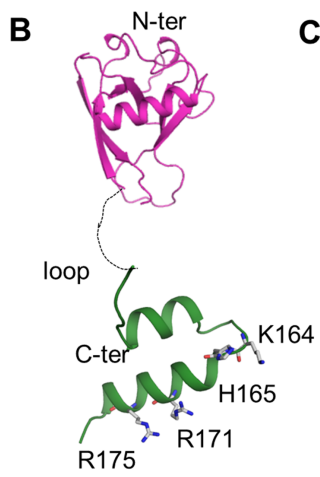
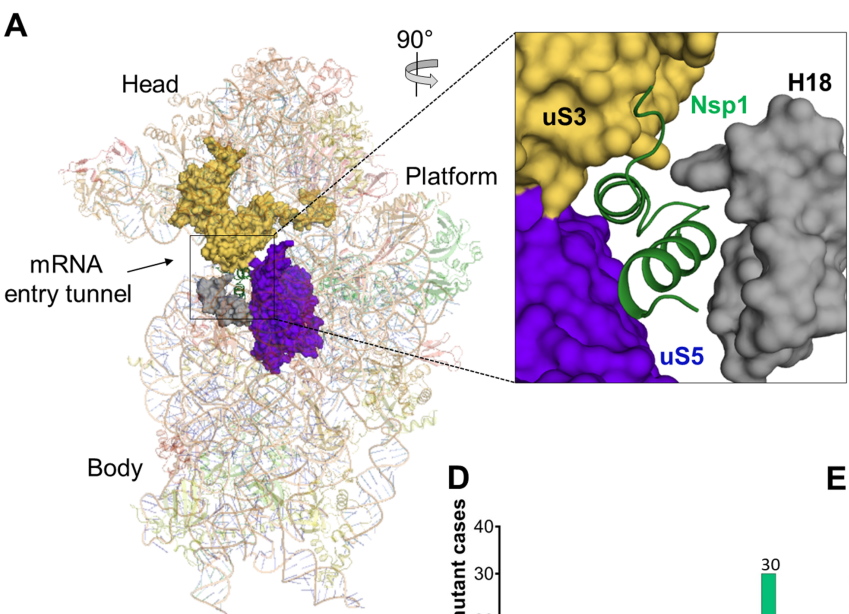


A**B****C****D**

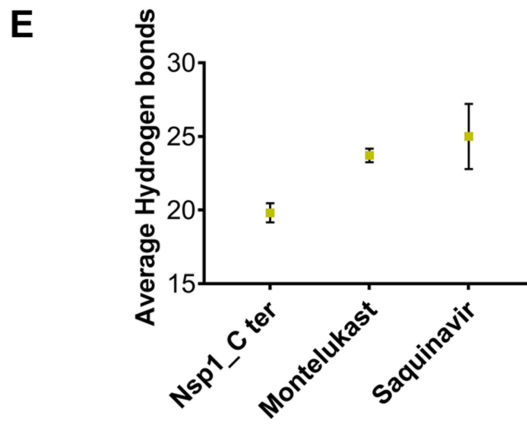
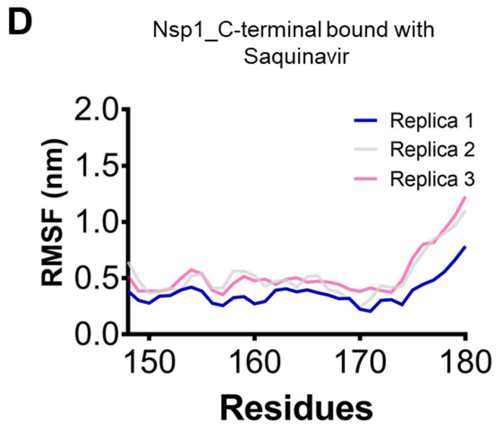
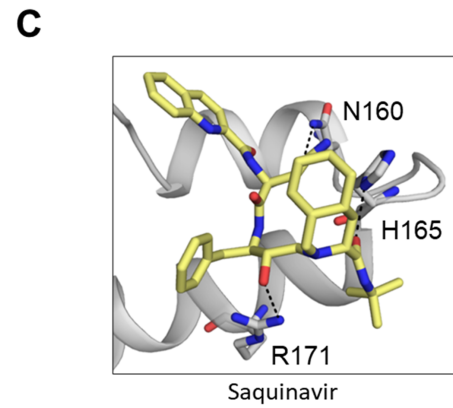
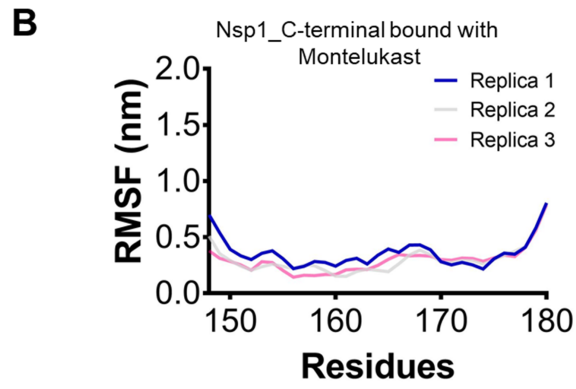
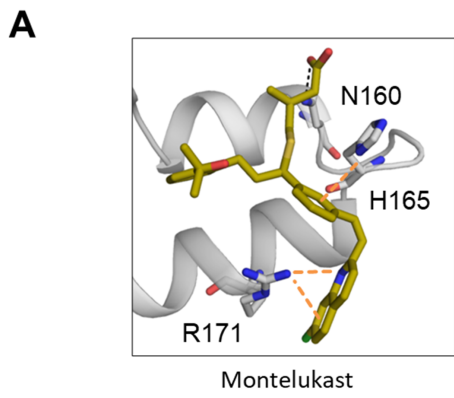
■ pcDNA (3.1) empty
 ■ *FLuc*+pcDNA (3.1) empty
 ■ *FLuc*+pcDNA-Nsp1
 ■ *FLuc*+pcDNA-Nsp1+Drug 50nM

■ *FLuc*+pcDNA-Nsp1+Drug 500nM
 ■ *FLuc*+pcDNA-Nsp1+Drug 1000nM
 ■ *FLuc*+pcDNA-Nsp1+Drug 1500nM
 ■ *FLuc*+pcDNA-Nsp1+Drug 2000nM

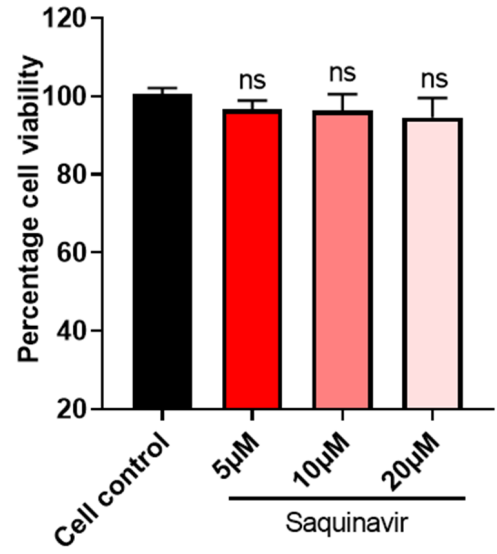
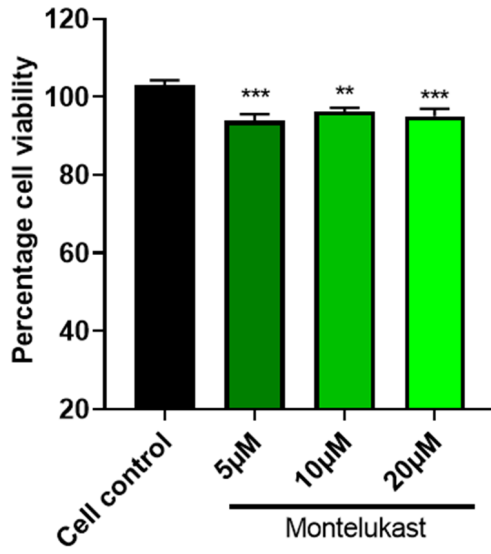
A**D****B****C****E****F**



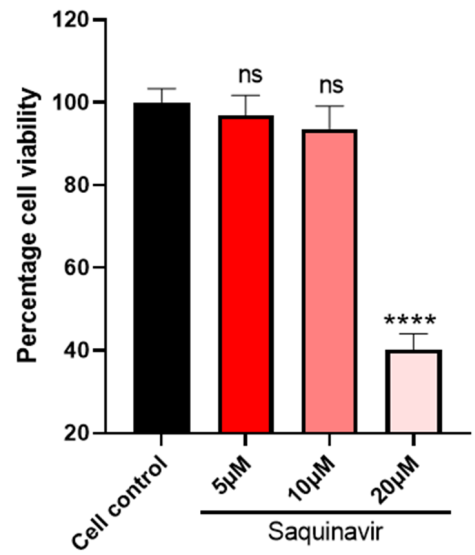
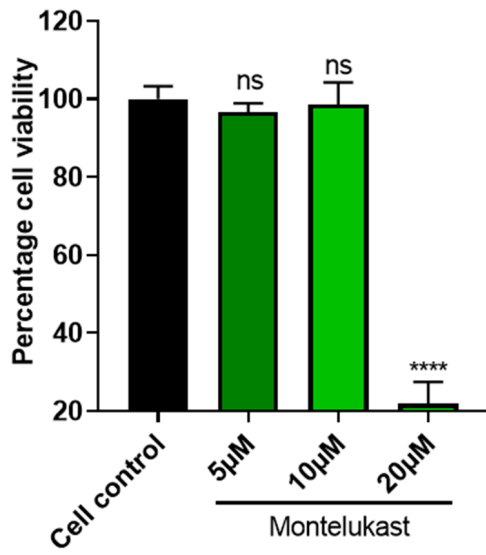
- | | | | |
|---------------|---------------|---------------|--------------|
| — Cloxacillin | — Perindoprin | — Nicardipin | — Mupirocin |
| — Saquinavir | — Bosentan | — Lidoflazine | — Verapmil |
| — Montelukast | — Dopexamine | — Doripenem | — Formoterol |

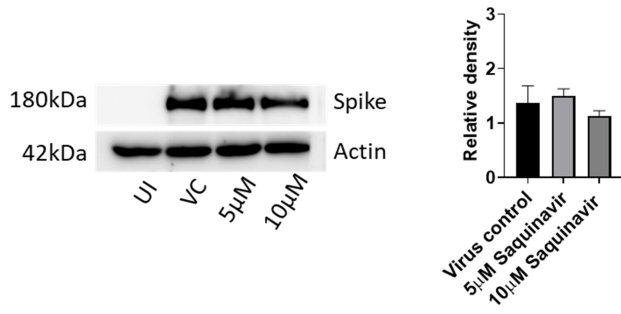
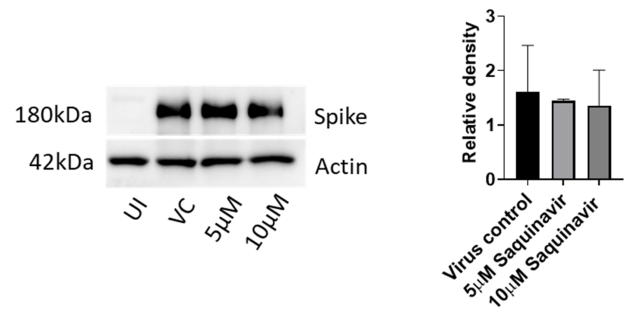
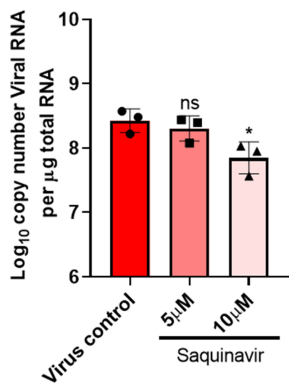
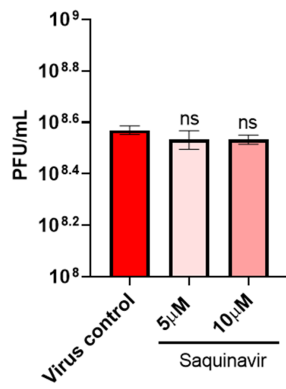
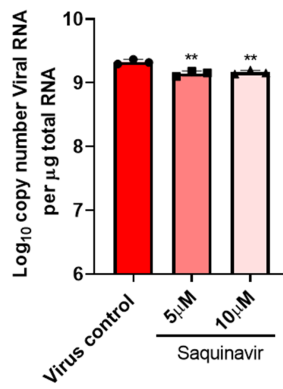


A



B



A**D****B****C****E****F**